Korean J. Chem. Eng., 38(8), 1592-1607 (2021)
DOI: 10.1007/s11814-021-0836-y

pISSN: 0256-1115
eISSN: 1975-7220

Thermo-hydraulic performance of nanofluids in a bionic fractal microchannel heat sink with traveling-wave fins

Cong Qi†, Liang Sun, Yuxing Wang, Chengchao Wang, and Genglin Chen

School of Electrical and Power Engineering, China University of Mining and Technology, Xuzhou 221116, China
(*Received 10 February 2021 • Revised 23 April 2021 • Accepted 3 May 2021*)

Abstract−Aiming at high working power and heat dissipation of electronic components, this study developed a novel bionic fractal microchannel heat sink with traveling-wave fins based on fractal theory and disk-like tree-like structure. α-Al_2O_3-water nanofluid was chosen as the working fluid instead of water in the microchannel heat sink. Thermo-hydraulic performance of nanofluids in the bionic fractal microchannel heat sink with traveling-wave fins was simulated numerically, and its comprehensive performance was studied. The main control parameters of this study include the depths of the traveling wave structure (h=0.00005 m, 0.00010 m, 0.00015 m, 0.00020 m, 0.00025 m), the eccentricity ratios of the traveling wave structure (e=0, 0.1, 0.2, 0.3, 0.4) and Reynolds numbers (Re=200-1,000). Results indicate that the surface temperature of the microchannel heat sink decreases with Reynolds number and depth of traveling wave structure. The use of traveling ribs at fractal corners can convert the inhomogeneous flow caused by the fractal effect into a stable horizontal channel flow more efficiently, while the temperature uniformity increases with depth and eccentricity ratio. Results also show that the traveling wave structure has the best overall performance when the eccentricity ratio of the traveling wave structure is 0.1 or 0.2, and the depth is 0.00020 m or 0.00025 m.

Keywords: Nanofluids, Bionic Microchannel Heat Sink, Traveling Wave Fin, Thermo-hydraulic Performance

INTRODUCTION

Since microelectronic chips are developing in the direction of smaller chip volume with higher heat flux density, heat dissipation has become pivotal in electronic chip design and application [1,2]. Microchannel heat sinks (MHS) are compact with high heat transfer performance, making them ideal for cooling microelectronic chips [3,4].

Tuckerman et al. [5] first used microchannels as a cooling method for electronic components in the 1980s. After that, flow and thermal exchange characteristics of microchannels were studied through experimental or numerical methods [6,7].

However, in the application process, it was found that although the microchannel can play a role in strengthening heat transfer while it will also bring about problems such as increased pump power; therefore, it is important to optimize the structure of the microchannel so that the flow resistance can be controlled within a reasonable range while improving the heat transfer effect [8,9].

In 1995, the concept of nanofluids was put first forward by Choi [10]. Nanofluid is a new type of heat transfer working fluid formed by mixing nanoparticles with traditional base fluids [11,12]. Therefore, nanofluids have higher heat transfer enhancement performance than ordinary working fluids. Because nanofluids have small thermal resistance and large thermal conductivity, a large number of in-depth researches have been made [13,14].

The concept of fractal was first put forward by French, Benoit Mandelbrot [15]. "Fractal in Latin refers to fragmented, irregularly fragmented objects. In 1997, a chip cooling radiator based on the construction theory and tree network structure was designed, and a fractal tree structure microchannel heat exchanger was also developed by Bejan and Errera [16]. Meanwhile, the enormous latent capacity of biomimetic fractal microchannels by combining structural theory and entropy generation principle was described [17]. Based on construction theory, a disk-shaped tree-shaped microchannel heat sink was proposed [18]. The working fluid flows from the center of the disk-shaped microchannels, then flows to all levels of channels. Through several simulation researches, it was widely accepted that a tree-shaped microchannel has a better heat dissipation effect and a more uniform temperature distribution than the traditional parallel microchannel [19,20].

Afterward, Chen and Cheng [21] conducted experimental research on the fractal tree-shaped microchannel heat sink. The experimental outcomes showed that the heat exchange effect of fluid in fractal microchannel heat sinks is more pronounced than that of parallel microchannel under the same heat flux density. Ma et al. [22] designed a branching microfluidic T-junction and numerically studied the asymmetrical breakup of droplets. Results showed that the more branches there are, the larger is the volume distribution ratio, which provided inspiration for the design of T-shaped microchannels. Dong et al. [23] studied a honeycomb shape fractal microchannel heat sink. The research outcome showed that the thermal exchange of the honeycomb fractal micro-pipe is more than five times that of the parallel micro-pipe heat sink, and the pump power is about 1/10 of the parallel micro-pipe. Emerson et al. [24] performed numerical simulations on a fractal tree network structure microchannel heat sink, then studied the influence of the number

†To whom correspondence should be addressed.
E-mail: qicong@cumt.edu.cn

of branches and structural parameters on the microchannel of the fractal structure in detail. Many studies have shown that the application of micro-channel structure in heat exchangers has excellent heat transfer performance [25,26].

A large number of experiments have further pointed out that the rib coupling structure in the microchannel heat sink can intensify the forced convection thermal exchange to a certain extent [27,28]. Therefore, the study of rib coupling structure is an efficient way to enhance the thermal exchange performance of microchannel heat sink, while much research on the design optimization of microchannel heat sink rib coupling structure has been conducted [29,30]. Herman et al. [31] did research on the unidirectional flow thermal exchange in a microchannel with curved blades. They found that an increase in current velocity in a curved blade would lead to a sharp increase in thermal exchange performance. Qi et al. [32] analyzed the effect of heat sink structure on thermal exchange performance and concluded that metal foam shows the most excellent performance since it has an excellent ability on enhancing thermal exchange area. Guzman et al. [33] numerically studied the thermal exchange and flow enhancement characteristics of microchannels with asymmetric wave walls, then further summarized the influence of wave wall amplitude and period on thermal exchange characteristics. Kim et al. [34] systematically investigated the generation of the vortex in the microchannels and their advantages and disadvantages, thus leading to a method of enhancing thermal exchange by engineering vortex generation. Qi et al. [35] experimentally studied the fluid flow and thermal exchange in elliptical tubes with a built-in turbulator. Results showed that the diverse axial ratio elliptical tubes have a significant effect on heat transfer enhancement due to the interruption and recomposition of the thermal boundary layer under the reinforcement of mainstream interference.

Through much research, it can be known that the fractal tree microchannel is a new type of heat sink structure inspired by the principle of bionics [36]. Its fractal tree network structure is optimal or close to the optimal shape formed after a long-term evolution process and has a strong heat and mass transfer capacity. Compared with the traditional microchannel heat sink, the fractal tree-shape microchannel heat sink has the advantages of small pres-

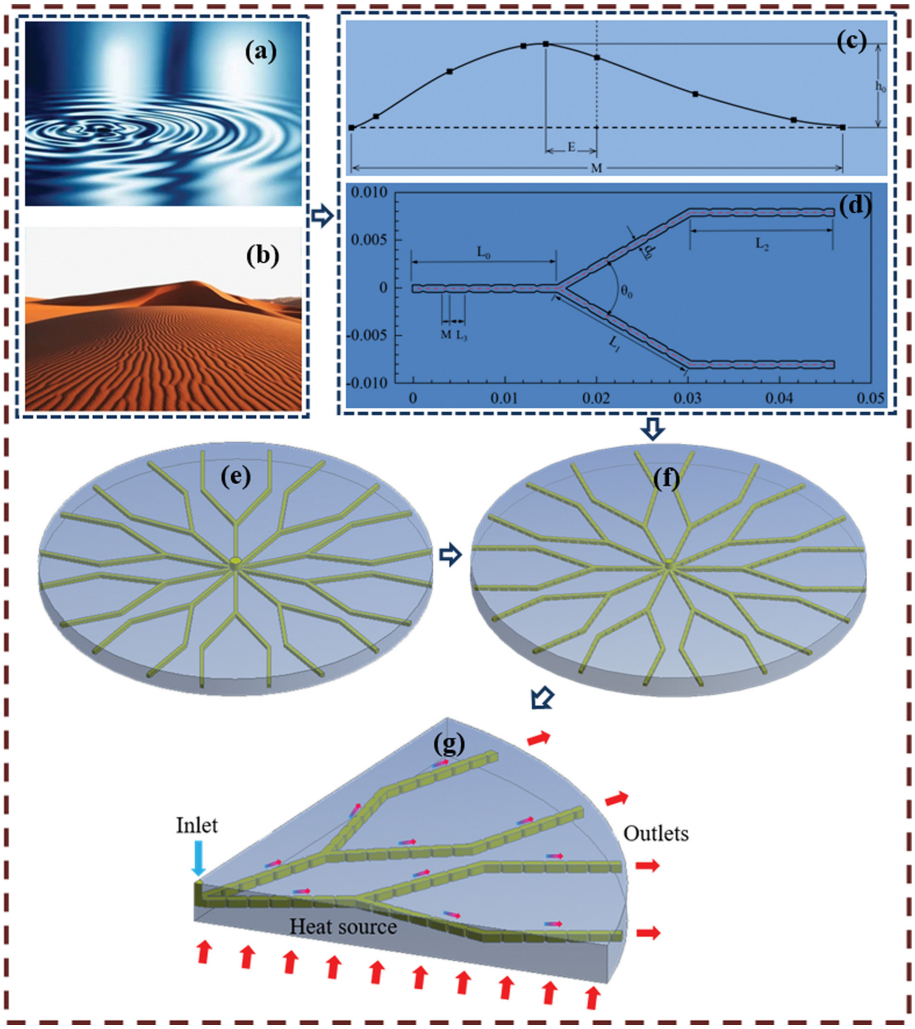

Fig. 1. Bionic tree-shape microchannel heat sink with bionic traveling wave rib. (a) Water surface ripple, (b) desert Gobi landscape, (c) Bionic traveling wave rib, (d) Detail structure of TMHS with bionic traveling wave rib, (e) TMHS, (f) TMHS with bionic traveling wave rib, (g) One-fifth of TMHS with bionic traveling wave rib.

sure drop, low thermal resistance, and relatively uniform temperature distribution [37,38]. At the same time, in the bionic fractal microchannel heat sink, the rib coupling structure will cause a virtual optimization, and the new heat exchange working medium nanofluids have high heat transfer capacity and will not cause blockage and wear of equipment [39,40]. Therefore, the application of nanofluids to fractal tree microchannels has become a new research direction [41,42].

Motivated by the above, based on fractal theory and disc-shaped tree-like microchannel structure, a new type of variable cross-section form traveling wave structure is established based on bionic optimization, which is less investigated and can deeply enhance the thermal exchange compared with the previous references. And this new bionic structure is combined with the fractal microchannel heat sink with nanofluids as the working fluid instead of water. The thermo-hydraulic performance of microchannel heat sink with different traveling wave design parameters has been numerically analyzed and its comprehensive performance also studied, which can provide the optimum size for the new tree-shape microchannel heat sink and provide a new idea for the design and development of new microchannel heat sink.

METHODOLOGY

1. Physical Model

Fig. 1 is the bionic fractal microchannel heat sink with bionic traveling wave rib. MHS represents "microchannel heat sink" and TMHS represents "tree-shape microchannel heat sink" in this study. By observing the ripples on the water surface and the landform of the Gobi desert, as shown in Fig. 1(a) and Fig. 1(b), it is found that the surface shape is a special wave-shaped structure, and this wave-shaped structure is perpendicular to the direction of the incoming flow and adapts to the local wind speed environment. According to Darwin's theory of natural evolution, the shape of the structure is most suitable for vertical fluid flow across the surface, so there is reason to believe that there is the possibility of pressure drop for this shape of the structure.

Hence, a new bionic traveling wave rib based on water surface ripple and Gobi desert landscape is developed in this study, which is shown in Fig. 1(c). h_0 is the height from the peak to the trough of the traveling wave structure, M is the width between the peaks of the structure, and E is the distance between the deepest point of the structure and the center of the structure. In this paper, the high-order multi-point spline curve is used to fit the wave shape with eccentricity. Due to the large aspect ratio of this design structure, 9-point control is adopted. The five control points on the left and right of the structure are equidistant, and the left and right parts have two upper and lower points, which are symmetric around the center point. To smooth the curve and reduce unnecessary pressure difference resistance, the depth displacement ratio between each control point and two adjacent control points should not exceed 3. The final design depth ratio is 1 : 3 : 3 : 1 on the left, the half part on the right is 1 : 2 : 2 : 1 while the curvature of each control point is continuously set to further smooth the curve.

The structure of the channel has a crucial influence on TMHS [43,44]. Fig. 1(d) tells the detailed structure of TMHS with bionic traveling wave rib. The radius of the heat sink is denoted as R, that of the entrance is denoted as R_{in}, respectively, and the fractal angle is set to 60°. Table 1 shows the main structural parameter selection and settings.

Table 1. Basic parameter setting

Variable	Parameter	Variable	Parameter
L_0 (mm)	17	M (mm)	0.5
L_1 (mm)	14.5	d_0 (mm)	1
L_2 (mm)	16	H (mm)	1
L_3 (mm)	2	θ_0	60°

TMHS has been studied deeply [45,46]. Peng et al. [47] presented a disk-shaped TMHS model which is the basis of the physical model in this study, as shown in Fig. 1(e). Three main parts make up this physical model: the top cover, the base with fractal grooves dug, and the thermal source connected to it.

Aiming at further improving the thermal exchange and reduce the pressure drop, the above bionic traveling wave rib was applied to the TMHS model, and a new TMHS model with bionic traveling wave rib is presented in Fig. 1(f). To speed up the convergence speed of numerical calculations, one-fifth of the TMHS with bionic traveling wave rib overall structure is shown in Fig. 1(g).

2. Theory

Several assumptions have been used to make the numerical calculation model more reasonable: (1) Steady laminar flow; (2) Incompressible, Newtonian, and viscous fluids; (3) Rough walls without velocity slips and temperature jumps.

The governing equations of the steady-state flow comprise the conservation laws of mass, momentum, and energy which are indicated below.

Mass conservation equation is shown in Eq. (1):

$$\nabla \cdot \nu = 0 \tag{1}$$

Momentum conservation equation is given by Eq. (2):

$$\rho(\nu \cdot \nabla)\nu = -\nabla P + \mu \nabla^2 \nu \tag{2}$$

Eq. (3) shows the energy conservation equation for fluid (α-Al_2O_3-water nanofluids as working fluid):

$$\rho C_{p,f}(\nu \cdot \nabla T) = \lambda_f \nabla^2 T \tag{3}$$

The energy conservation equation for solid (structure of TMHS) is expressed by Eq. (4):

$$\lambda_s \nabla^2 T = 0 \tag{4}$$

where ∇ is a Hamiltonian calculator, ν is the velocity vector, ρ is the density of the fluid, P is the pressure at a certain point inside the fluid, μ is the kinetic viscosity of the fluid, T is the temperature at a certain point inside the fluid, $C_{p,f}$ is the specific heat capacity of the fluid, λ_f and λ_s are the thermal conductive of the fluid and the solid respectively.

3. Numerical Method

The model is computed using the computational fluid dynamics (CFD) software Fluent, which uses the finite volume method to solve the discretization of the generated mesh by dividing the computational region into a series of non-repeating control vol-

umes. The finite volume method is based on a conservation equation in integral form rather than a differential equation, which describes each control body defined by the computational grid.

Copper was selected as the material for TMHS with thermal conductivity of 381 W/(m·k), a density of 8,900 kg/m^3, and a specific heat capacity of 386 J/kg·K. Copper is a non-ferrous metal with high thermal conductivity and excellent corrosion resistance in microchannel heat sinks, resulting in better heat transfer in microchannel heat sinks. Hence it is commonly used in experimental studies.

Knudsen number is used to determine whether the fluid is suitable for continuous assumption and is expressed by Eq. (5) with the mean free path of a particle being expressed by Eq. (6):

$$\mathrm{Kn}=\frac{\lambda_m}{\mathrm{L}} \tag{5}$$

$$\lambda_m=\frac{1}{\sqrt{2}\pi \mathrm{d}^2 \mathrm{n}_v} \tag{6}$$

where Kn is the Knudsen number, λ_m is the mean free path of a particle, L is the feature-length meaning the diameter of the microchannel here, d is the diameter of the microchannel, and n_v is the molecules per unit volume related to the concentration of the nanofluid.

Qi et al. [48,49] prepared α-Al_2O_3-water nanofluid and applied it to cool a general channel. The same nanofluid is adopted in this paper, and the type is TAP-A21 and its crystal shape belongs to α. Because α-Al_2O_3 nanoparticles have stable crystal phase and high thermal conductivity, it has a good heat dissipation effect. It is a kind of water-based nanofluid with a concentration of 0.09% and a particle size generally around 40 nm whose Knudsen number is 6.0072×10^{-10} by calculation, and its thermal properties have been determined experimentally. It is generally believed that when the Knudsen number is less than 0.001, the fluid flow belongs to the category of continuous media.

Therefore, α-Al_2O_3-water nanofluids under microchannel conditions were chosen and are consistent with the continuous medium hypothesis. It is ultimately considered as a single-phase fluid with the thermal conductivity of 0.7809 W/(m·k), the density of 1,264.661 kg/m^3, the specific heat capacity of 3,871.74 J/kg·K, and the viscosity of 1.271×10^{-3} kg/m·s. The thermal conductivity and specific heat capacity are obtained from the DRE-III multi-functional rapid thermal conductivity tester and the viscosity is obtained from the NDJ-5S digital viscometer while the density can be calculated from the concentration of the nanofluids.

The calculation of the inlet is chosen as a speed inlet given by different Reynolds number conditions, and its temperature is set to 297.15 K, which is the normal temperature used by thermostats in the laboratory. Each of the outlets is set as a pressure outlet, while the relative pressure is zero. Besides, a thermal fountainhead with a heat flux $q=10^5$ W/m^2 is exerted on the foot of the TMHS, and the up walls and out walls are assumed to be an insulating layer, while the two inner walls are each set to be symmetrical. The value of this heat flux is still derived from the general value of the power supply under laboratory conditions, to facilitate data comparison with future experimental work.

To effectively calculate speed and pressure, it is valid to choose the SIMPLE algorithm. The assumption of the velocity field and the pressure field are carried out independently in the SIMPLE algorithm, while the corrections to the assumed pressure field are obtained through the mass conservation condition of the velocity field. Under relaxation factors are given as follows to run SIMPLE algorithms: pressure item with 0.5, the dynamic item with 0.2, and volume fraction with 0.4.

Since this study was to calculate each performance of TMHS at a steady state, when the normalized residual is less than 10^{-6} for the flow equation and less than 10^{-7} for the energy equation, the calculation is considered to be convergent.

4. Grid Independence Test and Model Validation

A grid independence study was conducted to reduce the calculation time and obtain a reasonable grid size, and four grid sizes (0.1, 0.05, 0.01, and 0.005 mm) were selected for the smooth TMHS-based model at a Reynolds number of 200. In the results, the maximum temperature differences between the inlet and outlets and the maximum pressure drop in the channel were contrasted, and the outcomes shown in Table 2, where ΔT is the maximum temperature difference between the inlet and outlets and ΔP is the maximum pressure drop in the channel.

Taking an element size of 0.005 mm as the benchmark, the differences are the relative errors between other grid sizes (0.1 mm, 0.05 mm, 0.01 mm) and the grid size 0.005 mm. Between the element size of 0.1 mm and 0.005 mm, the deviation of pressure drop and temperature rise is 0.506% and 0.227%, respectively. For the element size of 0.05 mm, the deviation has turned to 0.449% and 0.021%. However, when the grid size continues to decrease to 0.01 mm, the deviations of pressure drop (0.402%) and temperature rise (0.041%) are close to that of the element size of 0.05 mm. Hence, the calculation of a grid size of 0.05 mm is sufficiently accurate. With sufficient computational accuracy, reducing a certain number of grids can effectively improve computational speed and computational efficiency. Therefore, all calculations will be performed using a grid with an element size of 0.05 mm, thereby reducing the computational load while ensuring the accuracy of the calculation.

The final grid of the fractal microchannel is laid out by mesh

Table 2. Grid independence test of the TMHS

Element size (mm)	Mesh number	ΔP (Pa)	Difference	ΔT (K)	Difference
0.1	1,911,180	200.76291	0.506%	31.65173	0.227%
0.05	2,715,519	200.87722	0.449%	31.71724	0.021%
0.01	15,691,518	202.59541	0.402%	31.73659	0.041%
0.005	28,921,487	201.78374	-	31.72378	-

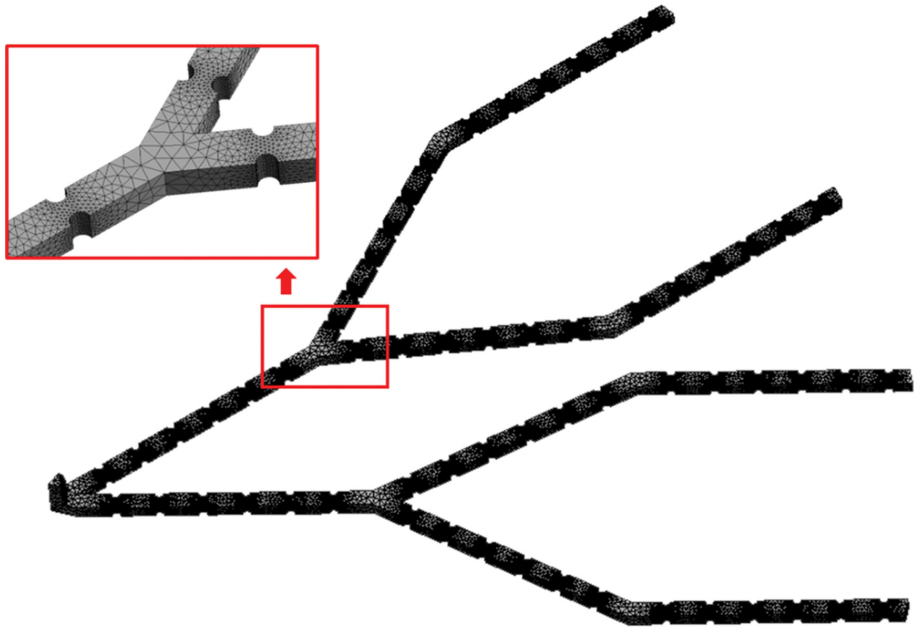

Fig. 2. Computational domain mesh.

and grid generation software for CFD Ansys Meshing in Fig. 2, where the mesh shape is mainly tetrahedral with an element size of 0.05 mm and the mesh is densified at the ribs.

The study calculates the overall heat transfer in the microchannel and the fluid flow in the channel at a steady state, with a calculation time of about 300 to 600 minutes for each operating condition, which increases slightly with the increasing Reynolds number.

To measure the reasonableness of the simulation outcomes, it is necessary to compare the numerical results of the outlet temperature with the numerical results obtained from the model proposed by Yan et al. [50] and the theoretical calculation results [51]. The theoretical outlet temperature can be calculated easily by using the equation of equilibrium $Q=C_p m\Delta T$, which shows the relationship between outlet temperature and Reynolds number [51]. Where C_p is the specific heat capacity of the fluid, m is the mass flowing through the TMHS at a certain time which can be calculated by Reynolds number, ΔT is the maximum temperature differences between the inlet and outlets, and Q is the heat gained by TMHS in a certain time.

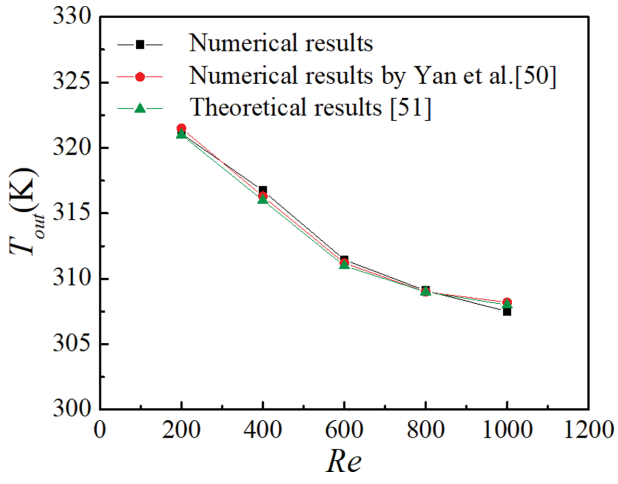

Fig. 3. Outlet temperature comparison.

Fig. 3 tells the comparison among the numerical values of the simulated outlet temperature under different Reynolds numbers, the numerical result obtained from the model proposed by Yan et al. [50], and the theoretical result [51]. The numerical simulation and theoretical outcomes [51] are consistent, while the maximum relative error is only about 1.336%, and the maximum relative error between the numerical result and the numerical result by Yan et al. [50] is only 0.527%. Accordingly, it shows the reasonableness and efficacy of the method.

5. Performance Evaluation

To simplify the expression for the design variables, an expression for the eccentricity ratio is introduced by Eq. (7):

$$e=\frac{E}{M} \tag{7}$$

The dimensionless number, inlet Reynolds number, is defined by Eq. (8):

$$Re=\frac{\rho uD}{\mu} \tag{8}$$

where ρ and μ are the density and dynamic viscosity of the working fluids, while u and D are the entrance velocity and channel diameter.

Thermal exchange performance is analyzed by the heat transfer coefficient and Nusselt number calculated by Eq. (9) and Eq. (10), respectively:

$$h=\frac{Q}{A\Delta T}=\frac{1/12\pi R^2 q}{A(T_s-T_f)} \tag{9}$$

$$Nu = \frac{hD}{\lambda_f} \tag{10}$$

where R is the radius of the TMHS, q is the heat flux density applied to the heated surface, A is the contact area between the inner wall of the TMHS and the fluid, T_s and T_f are the bulk temperatures of the solid and fluid regions, and λ_f is the thermal conductivity of the working fluids.

For radiator systems, the higher the pressure drop that emerged, the larger the pumping power required. The pressure drop and pumping power are calculated with the following Eq. (11) and Eq. (12), respectively:

$$\Delta P = P_{in} - P_{out} \tag{11}$$

$$Q_{pum} = \Delta P \cdot U \tag{12}$$

where P_{in} is the inlet pressure while P_{out} is the outlet pressure, with U is the volume flowrate.

To take into account the effects of thermal exchange and pressure drop together, the evaluation standard of heat exchanger performance η is calculated using the following Eq. (13):

$$\eta = \frac{Nu/Nu_{sm}}{(\Delta P/\Delta P_{sm})^{1/3}} \tag{13}$$

where Nu_{sm} and ΔP_{sm} are the average Nusselt number and pressure drop of the smooth wall surface TMHS.

RESULTS AND DISCUSSION

1. Contrastive Analysis of Flow Characteristics

Thermal exchange characteristics in the channel flow are significantly affected by the flow model of the fluid [52,53]. In this part, the flow characteristics are mainly analyzed in detail. For the fractal microchannel, when the fluid flows into the fractal channel, a stagnant area of fluid flow occurs. This area is mainly concentrated next to the outer wall, which will result in higher thermal exchange performance near the inner wall while lower thermal exchange performance near the outer wall. This phenomenon is generally called the fractal effect. The obvious branch will enhance the heat transfer performance, while the fractal effect will generate certain thermal stress in the material due to the uneven heat dissi-

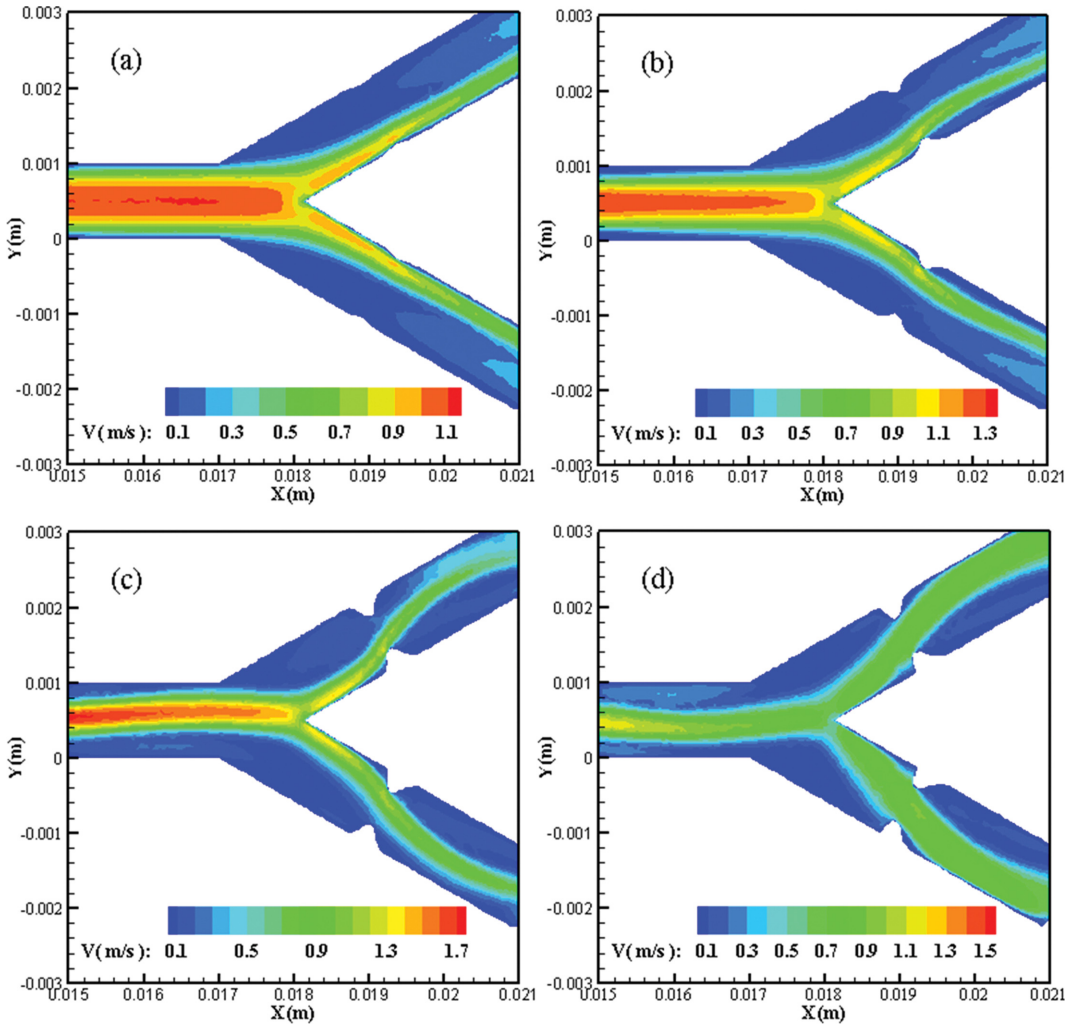

Fig. 4. Velocity contours on the middle planes of the first-order fractal corner at Re=600. (a) h=0.00010 m, e=0.1, (b) h=0.00015 m, e=0.1, (c) h=0.00025 m, e=0.1, (d) h=0.00025 m, e=0.3.

pation effect inside and outside the channel. Therefore, the strength of the fractal effect is the evaluation standard of thermal exchange performance.

According to the fluid flow mode, the degree of flow in the channel, and the overall structure of the sub-typed micro-channel, the flow state of the nanofluids in the micro-channel will be investigated from two aspects: first-order sub-flow angle and second-order sub-flow corner. The first-order fractional flow angle refers to the position where the main flow channel of the channel first fractals into two tributaries and the second-order fractional flow angle refers to the 150° corner when the oblique direct current is converted to parallel mainstream flow.

1-1. The Flow of the First-order Fractal Corner

It can be seen from Fig. 4 that after the first-order fractal corner, the maximum speed has been significantly increased and it appears directly behind the ribs. The injection of the ribs narrows the channel so that when the fluid flows from a large flow area into a narrower flow area, a greater flow velocity is obtained. Also, it can be found in Fig. 4 that disturbance causes the streamline to be interrupted and redeveloped at the ribs, and the interruption and redevelopment occur repeatedly between the corresponding ribs after the first corner.

The introduction of the fins not only increases the speed value but also changes the floating direction and mode, thereby improving the overall development of the fluid flow in the channel as a whole. From the perspective of the flow boundary layer, after adding ribs, the thickness of the inner boundary layer of the pipeline increases, while the thickness of the outer boundary layer decreases. Thus, the introduction of ribs can suppress internal heat transfer and enhance external heat transfer. The accompanying wave-shaped ribs increase the flow disturbance of the main channel. After passing the first-order fractal corner, the flow range of the fluid is wider and the outer boundary layer is further thinned, which enhances the heat transfer outside the fractal channel and effectively suppresses the fractal effect. At the same time, as the eccentricity ratio increases, the angle of the windward slope increases while the boundary layer on the leeward slope gradually thickens so that the overall flow resistance decreases.

1-2. The Flow of the Second-order Fractal Corner

At the second-order fractal corner, due to its flow characteris-

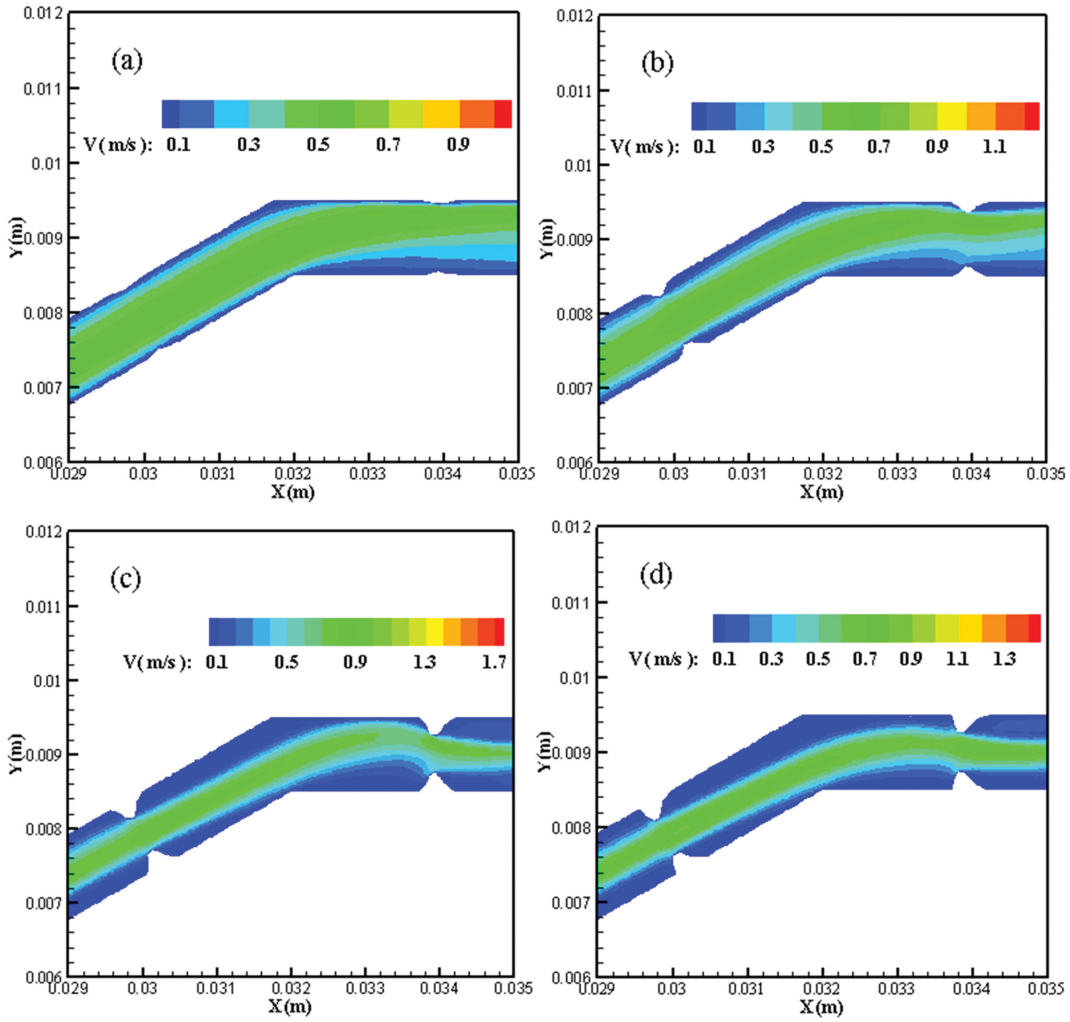

Fig. 5. Velocity contours on the middle planes of the second-order fractal corner at Re=600. (a) h=0.00010 m, e=0.1, (b) h=0.00015 m, e=0.1, (c) h=0.00025 m, e=0.1, (d) h=0.00025 m, e=0.3.

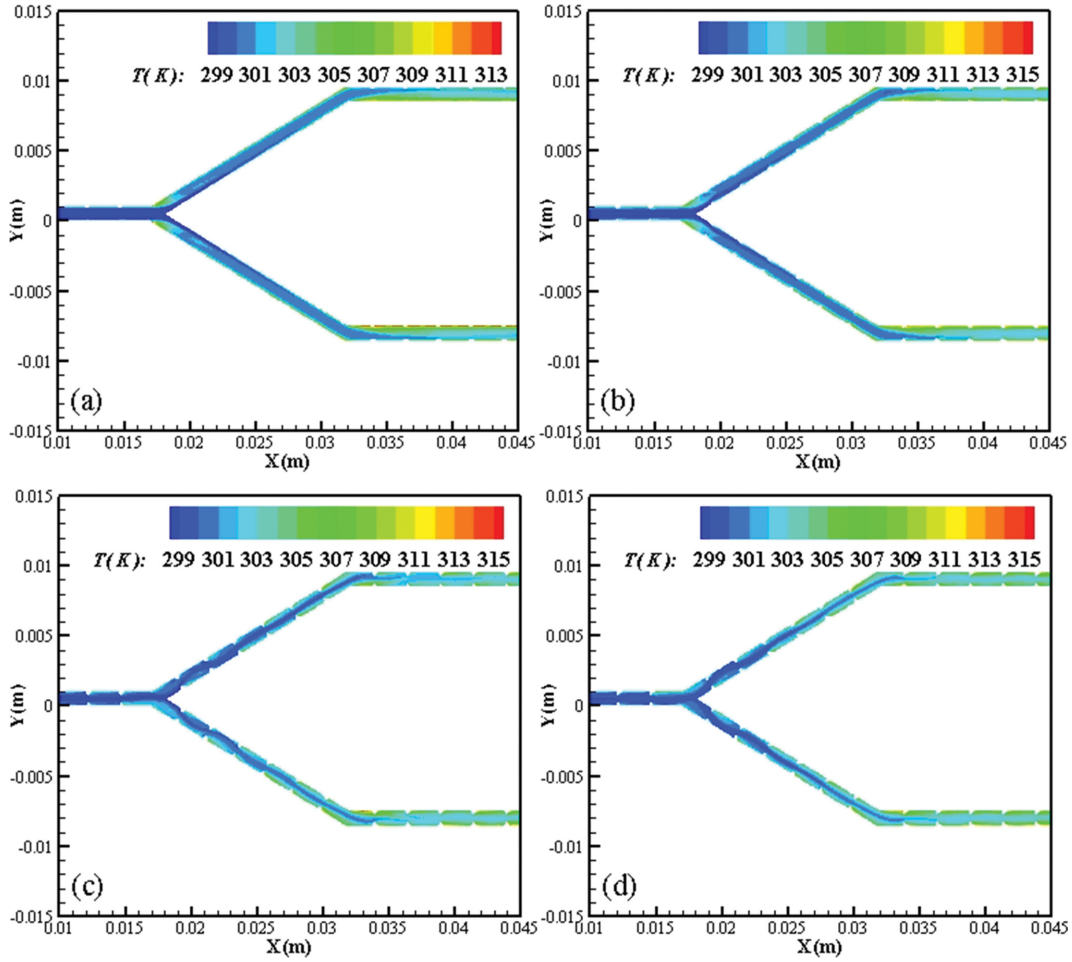

Fig. 6. Temperature distribution on the middle planes of the channels at Re=600. (a) h=0.00010 m, e=0.1, (b) h=0.00015 m, e=0.1, (c) h=0.00025 m, e=0.1, (d) h=0.00025 m, e=0.3.

tics, Fig. 5 mainly shows that the outer heat transfer effect is better, the boundary layer is thinner, and the inner boundary layer is thicker, and the heat transfer capacity is poor. Therefore, after the second-order fractal corner, there will be a large external friction resistance and a high internal local temperature. The introduction of a traveling wave rib can destroy the outer flow and achieve disturbance, increase the thickness of the outer boundary layer, reduce the pressure drop, and destroy the inner boundary. The continuous regeneration of the boundary layer can enhance the heat transfer and achieve uniform temperature. At the second-order fractal corner, the main damage of the boundary layer is caused by the fractal effect of the outer stable flow, which destroys the outer flow, and because of the structural advantages of the traveling wave ribs, the flow regeneration will be relatively simple and fast.

In general, using traveling wave ribs at the second-order fractal corner can more efficiently transform the uneven flow caused by the fractal effect into a stable horizontal channel flow.

2. Contrastive Analysis of the Thermal Exchange Characteristics

The most obvious manifestation of the heat transfer effect is the temperature distribution of the fluid and TMHS [54,55]. To highlight the optimization of the heat transfer effect of the traveling wave ribs on the fractal TMHS, the following will proceed from the two aspects of the fluid temperature in the channel and the overall plate temperature distribution. By comparison, it can be seen that the traveling wave rib has various heat transfer optimization effects on the fractal TMHS.

As we can see in Fig. 6, the temperature of the main flow channel gradually decreases at the sidewall temperature near the mid of the channel and, accordingly, the fluid temperature gradually increases. After flowing into the branch channel, the higher fluid temperature has a higher temperature gradient and the fluid temperature near the outer wall has a significant increase, which is lacking the help of the mainstream low-temperature flow. However, as the fluid temperature gradually averages and decreases, the temperature gradient becomes smaller and the maximum temperature gradient appears in the stagnant area near the outer wall.

After introducing the traveling wave ribs in the microchannel, the vicinity of the thermal boundary layer wall, especially the outer wall, is regenerated and a higher temperature gradient is obtained. Besides, the heat on the boundary is continuously carried into the mainstream for the reason of continuous interruption and recomposition of the boundary layer, the temperature of the mainstream gradually rises and a more symmetrical fluid temperature

distribution relative to the centerline is obtained. Therefore, the wake temperature of the TMHS main runner with the traveling wave ribs is higher than the wake temperature of the smooth TMHS. With regard to the fractal channel, it is found that the inner temperature gradient raises, but the outer temperature gradient drops and is relatively smoother. This is because the introduction of the traveling wave ribs effectively suppresses the fractal effect and achieves convergence of inner and outer flows.

It can be seen that when there are no traveling wave ribs or the depth of the traveling corrugated ribs is very small, the local high-temperature points will propagate more obviously on the outside of the first-order fractal angle and the inside after the second-order fractal angle. As the rib is introduced and the rib depth increases, the temperature difference decreases, which means increasing flow disturbances are occurring. At the same time, this also shows that the expansion effect leads to an increase in the flow rate and an increase in the recirculation rate, which leads to a thinning of the boundary layer, a decrease in heat transfer resistance, and an increase in heat transfer efficiency. When the fluid enters the fractal channel, the outer boundary layer becomes thinner, which enhances the heat dissipation inside and outside the fractal channel, reduces the overall temperature of the wall surface, reduces the temperature of local high-temperature points, and reduces the range of local high-temperature points. Similarly, as the Reynolds number increases, the heat dissipation effect is optimized and the local high-temperature points of the entire channel are greatly reduced. The effect of the eccentricity ratio on the temperature distribution effect in the tube, especially the effect of the fractal corner, is not obvious. The local high-temperature points have a huge impact on the microchannel. Effectively controlling the scale of the local high-temperature point in the fractal microchannel can control the thermal stress in the channel to a great extent. By adding traveling wave ribs, the local high-temperature problem in the channel especially at the fractal corners can be solved ingeniously.

For the overall layout temperature distribution, Fig. 7 compares the temperature change and the isotherm development of the entire radiator under the same Reynolds number and eccentricity ratio. The highest temperature and temperature evenness of the heat sink surface are major quotas for appraising the effect of the TMHS. Due to the structural characteristics of the fractal microchannel and the flow mode of the fluid in the channel, the overall temperature distribution of this type of microchannel plate surface can be determined by the layers of near-circular isotherms. The change in the form of the isotherm has little difference from the change of the eccentricity ratio, but the overall temperature

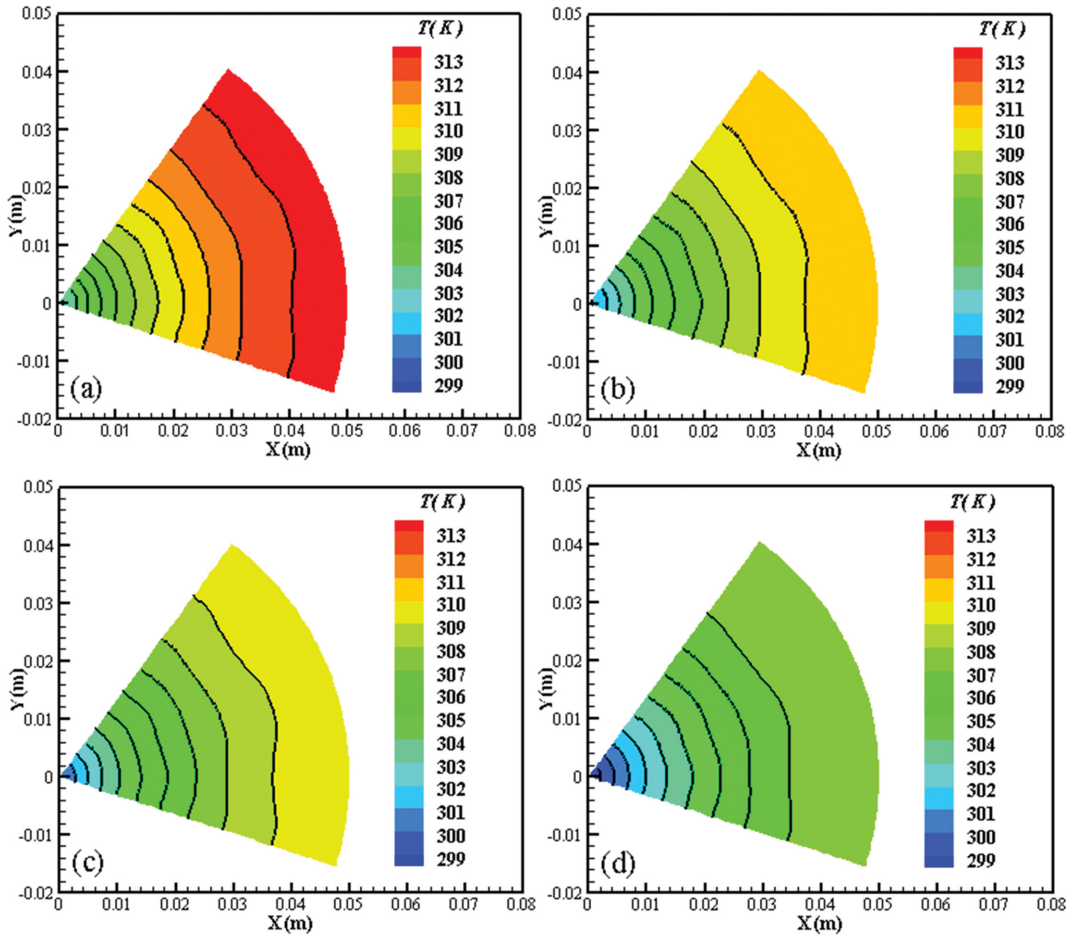

Fig. 7. Temperature distribution on the bottom surface planes of the TMHS at Re=600. (a) h=0.00010 m, e=0.1, (b) h=0.00015 m, e=0.1, (c) h=0.00025 m, e=0.1, (d) h=0.00025 m, e=0.3.

changes much. With the increase of the fluid Reynolds number, the overall isotherm tends to be more concentrated towards the center.

With the increasing depth of the traveling ribs, it is obvious that the maximum temperature of the plate surface gradually decreases, and the isotherm of the class of circular ring is gradually deformed, forming a kind of wave-like ring containing a protruding peak toward the center of the circle. This wave-like ring can be used as an important indicator to measure the uniformity of the layout. When the crest of the wavy ring isotherm rises continuously, the isotherm near the center of the plate surface is still more concentrated, which means that the outer main temperature zone is expanded and the overall temperature is more even. As shown in the figure, in the process of increasing the depth of the traveling ribs, the raised crest of the outermost isotherm gradually steepens as the overall temperature decreases, and the effect is most obvious when the depth of the traveling ribs reaches 0.00025 m when the area of the outer isotherm reaches the maximum.

The main reason for this phenomenon is that the disturbance caused by the traveling ribs plays a key role in intensifying the heat transfer in the more inhomogeneous flow at the end of the channel. According to the previous section, the flow of fluid in the fractal TMHS becomes progressively more inhomogeneous due to the fractal effect and the ribs at the end play a pivotal role in reinforcing the flow. Therefore, a higher thermal exchange effect and a more even temperature distribution are formed on the outer side of the overall plate, where is also the end of the fractal microchannel.

3. Contrastive Analysis of the Pressure Drop

Fig. 8 shows the variation of the pressure drop across the TMHS with the eccentricity ratio under different Reynolds number conditions and different traveling rib depths. It can be seen that as the depth of the ribs increases with the traveling wave, the overall pressure drop shows a relatively rapid increase, which is because the

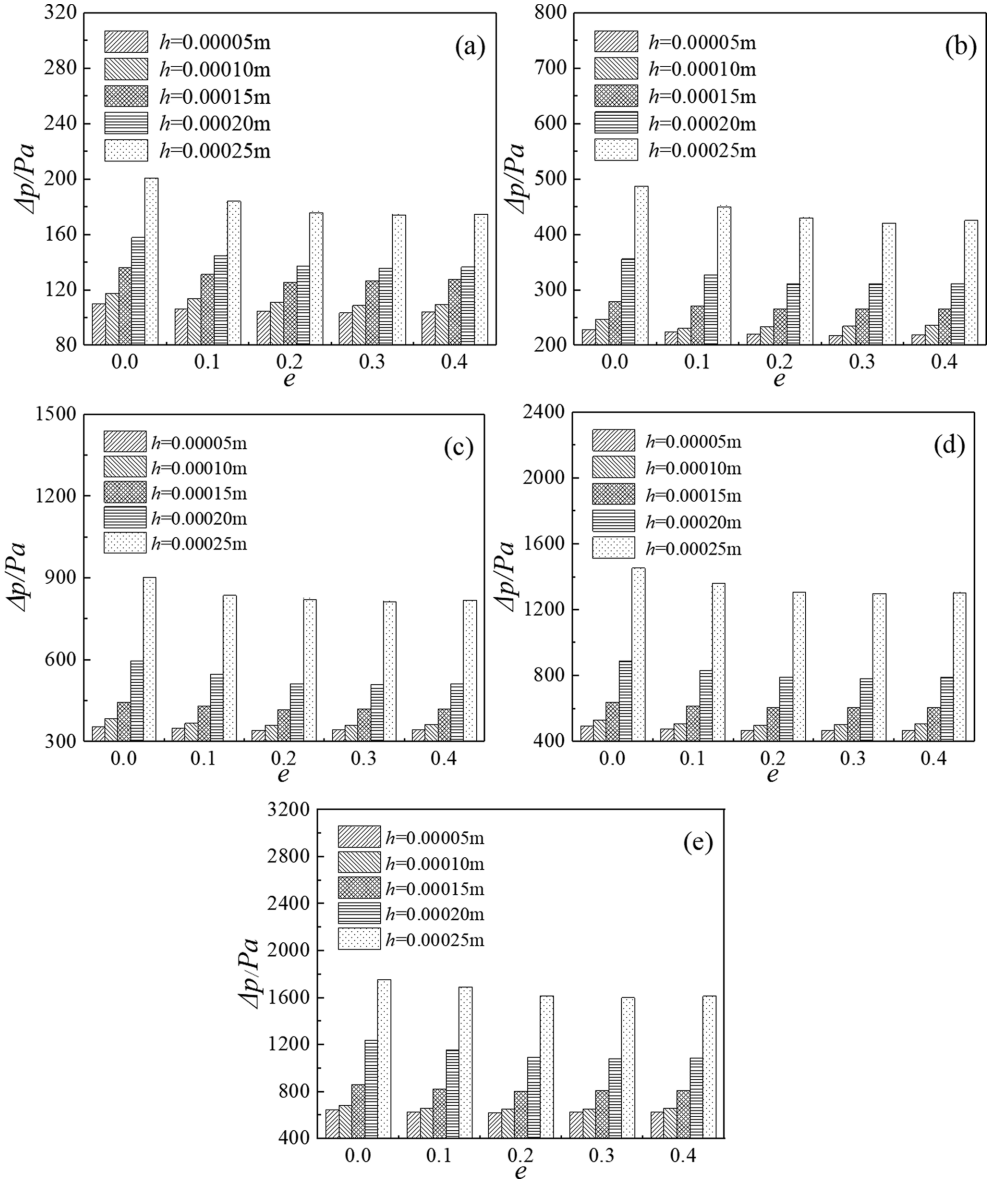

Fig. 8. Pressure drop versus eccentricity ratio. (a) Re=200, (b) Re=400, (c) Re=600, (d) Re=800, (e) Re=1,000.

presence of the ribs enhances the heat transfer at the cost of disturbing the fluid and repeatedly destroying the boundary layer, and as the depth of the ribs increases the higher the intensity of the boundary layer being destroyed, which leads to an increase in the overall pressure drop. This phenomenon has seen some changes with the introduction of traveling wave ribs. In conventional TMHS and normal ribbed TMHS, the first thing that occurs is the uneven distribution of pressure, especially at the location where the fractal effect occurs and the outer side of the channel brings a huge resistance and pressure drop. And with the application of traveling wave ribs in TMHS, the pressure drops rapidly with the contraction of the flow channel, which also shows the great influence of the ribs on the pressure. Upon entering the fractal channel, the traveling wave ribs can inhibit the fractal effect and form a more even flow and relatively even pressure distribution. Thus, the combined effect of branch and rib can reduce the pressure drop and thus mitigate the pressure drop caused by the ribs.

Further analysis of the above figure reveals that the traveling rib form with an eccentricity ratio of 0.1 exhibits a smaller pressure drop than various other eccentricity ratios under various conditions, especially compared to a common curved convex surface. That is because, with the introduction of the traveling wave ribs, the original flow state is disrupted when the fluid flows through the ribs. And because of the special shape of the traveling wave ribs, when the fluid flows from the crest to the trough, the first half of the structure on the leeward slope is a low-pressure area where the fluid boundary layer is gradually re-formed, while the second half of the fluid will gradually form a relatively stable flow again; and when it passes the trough it is about to experience the windward slope, where is a high-pressure area. The fluid will be accelerated from the peak to the trough of the wave, and because of the reverse pressure gradient the downward flow is controlled so that

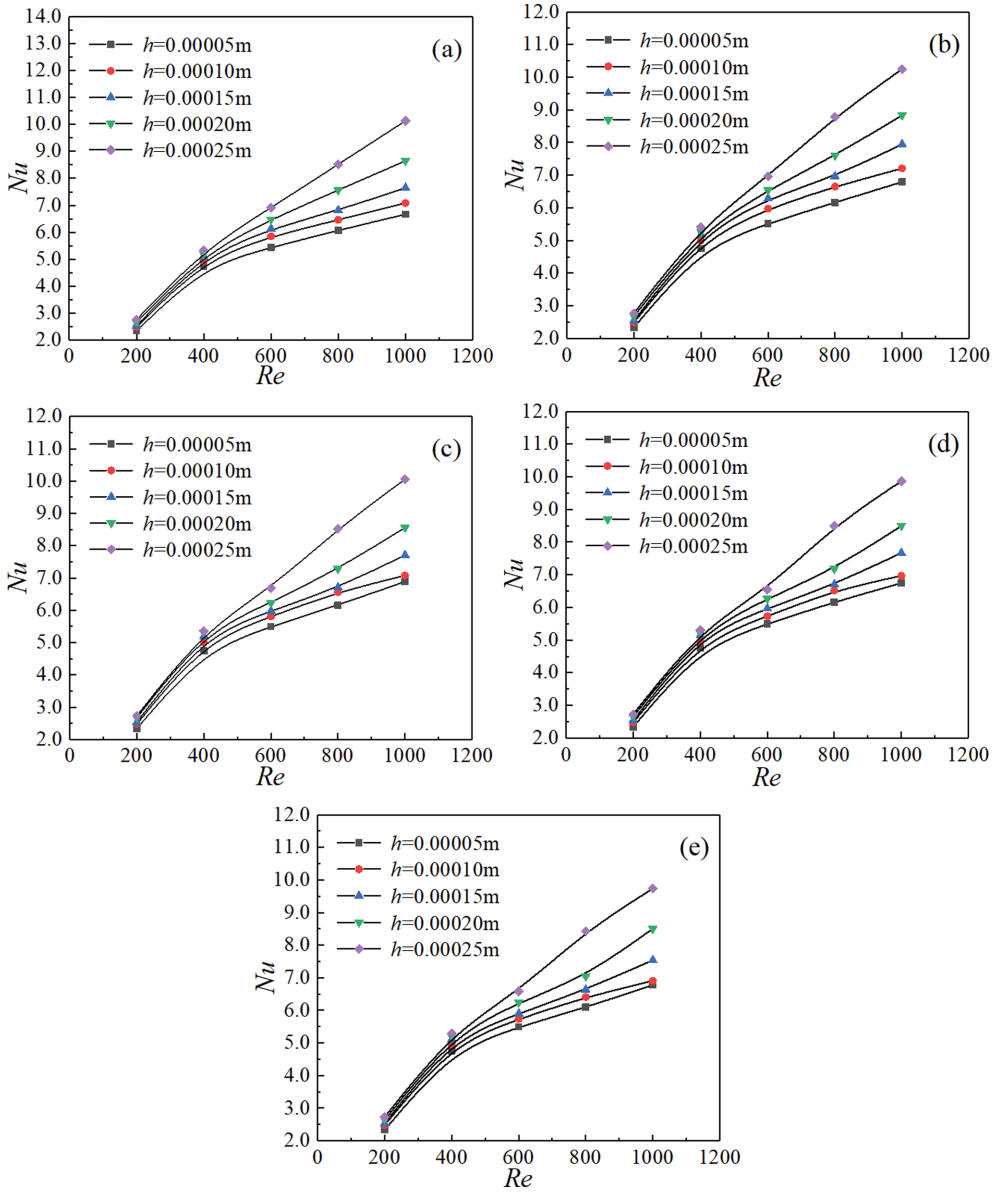

Fig. 9. Nusselt number versus Re. (a) e=0, (b) e=0.1, (c) e=0.2, (d) e=0.3, (e) e=0.4.

it is reduced and the pressure drop is reduced, so as to achieve a certain effect of reducing the pressure drop. However, as the eccentricity increases, the proportion of fluid colliding perpendicularly with the upwind direction increases and less fluid can be buffered, when the fluid available to re-form a stable boundary layer is further reduced, leading to an increase in pressure drop. With the increase of eccentricity ratio, the resistance reduction effect of pressure drop can be increased from 8.81% to 13.63%, and the resistance reduction effect decreases with the increase of Reynolds number.

4. Comprehensive Performance

Changes of Nusselt number with the variation of Reynolds number and eccentricity ratio are shown in Fig. 9 and Fig. 10, respectively. Results reveal that the heat transfer enhancement effect is similar to the pressure drop control effect described above. As the Reynolds number increases, the TMHS with traveling wave ribs under the same depth shows a parabolic-like increase in the Nusselt number, and the deeper the channel the steeper the Nusselt number growth curve. This indicates that the increase of traveling wave ribs has a relatively better effect at high Reynolds number conditions, which is due to its ability to form larger flow disturbances and faster boundary layer destruction and regeneration at high Reynolds number conditions.

Corresponding to the pressure drop, with the change of eccentricity ratio, the Nusselt number of TMHS with traveling wave ribs shows a trend of first increasing and then decreasing, and it is obvious at deeper rib depth and higher Reynolds number conditions. According to the analysis of the flow state, the fluid boundary layer has a better damage and regeneration state after the intro-

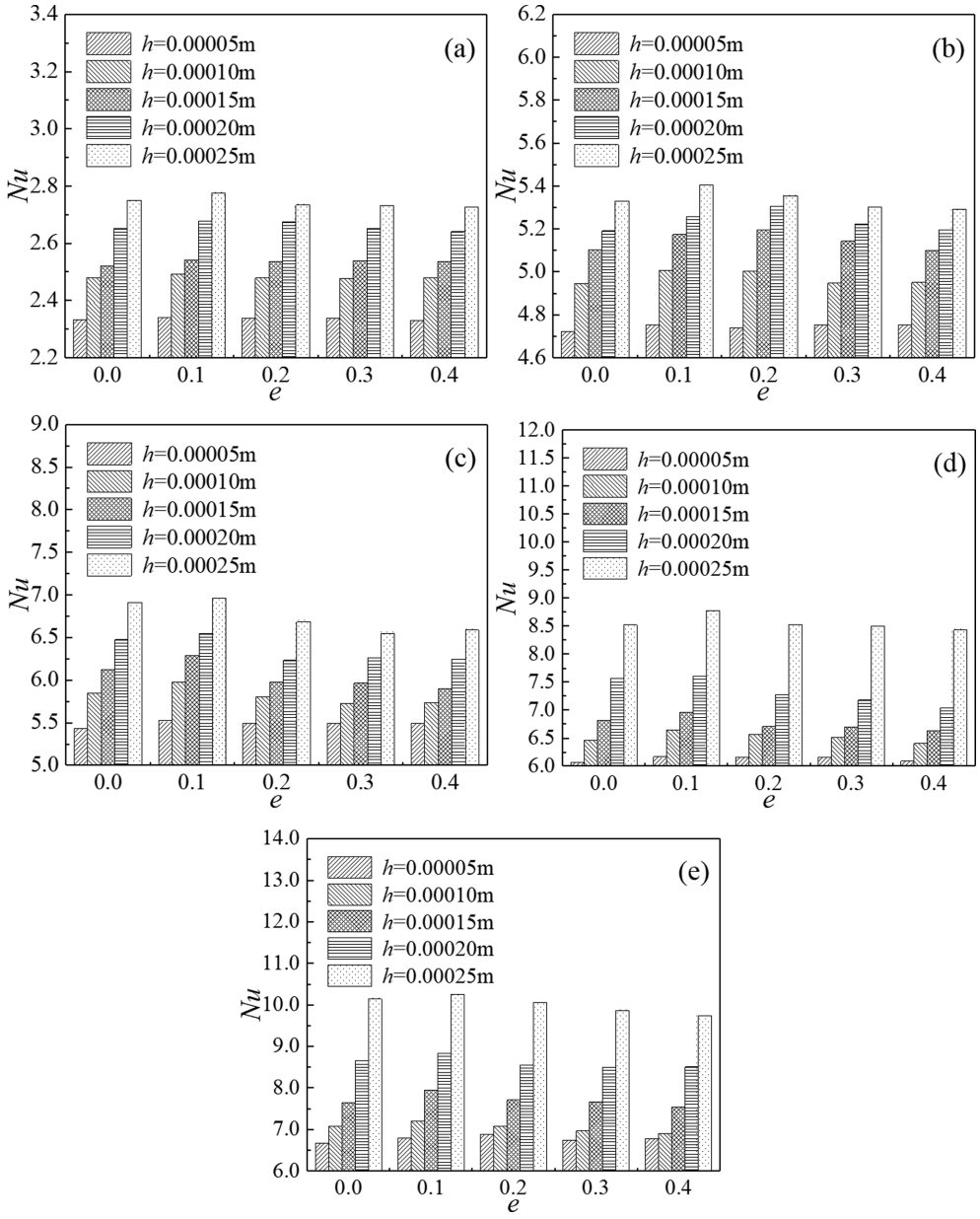

Fig. 10. Nusselt number versus eccentricity ratio. (a) Re=200, (b) Re=400, (c) Re=600, (d) Re=800, (e) Re=1,000.

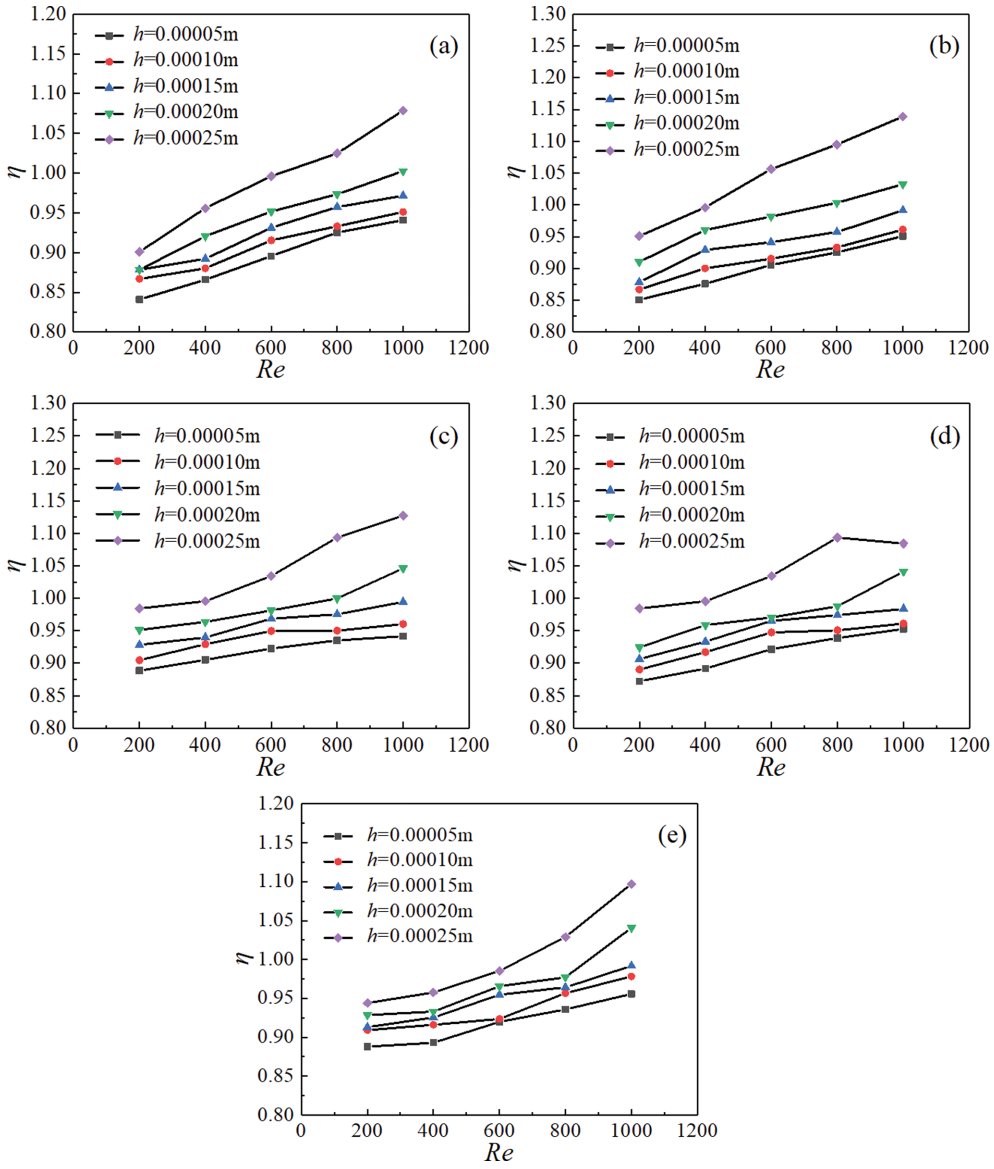

Fig. 11. η versus Re. (a) e=0, (b) e=0.1, (c) e=0.2, (d) e=0.3, (e) e=0.4.

duction of the traveling wave ribs, but as the eccentricity ratio continues to increase, the windward slope of the traveling wave ribs gradually steepens, causing the Nusselt number to be decreased by 2.10% to 5.58% instead.

Changes of efficiency with Reynolds number under different eccentricity ratios are presented in Fig. 11, where the efficiency of the small-depth traveling-wave rib TMHS varies less, mainly less than 1, indicating that the pressure drop caused by the small-depth traveling-wave ribs has a greater impact and cannot completely offset its ability to enhance heat transfer. For the large depth traveling wave rib TMHS, the efficiency increases gradually with the increase of inlet velocity. A higher Reynolds number means a higher value of flow velocity and a higher intensity of secondary flow, which improves the heat transfer and thus can be offset or even optimized with the effects generated by viscous forces. The overall efficiency is slightly worse than that of the smooth tube when the Reynolds number is low because the ribbed tube produces a larger pressure drop [56]. In the simulated Reynolds number range, the overall performance of the traveling wave rib is better than that of the normal arc rib. Among them, the TMHS of traveling wave ribs with eccentricity ratios of 0.1 and 0.2 can not only show 6.48% to 9.25% more efficient overall than TMHS with other eccentricity ratios at high Reynolds number conditions, but also the overall efficiency is not bad at low Reynolds number conditions, so they are considered to have better overall performance.

5. Contrastive Analysis on Working Fluids

The working fluids used in this study are mainly nanofluids because of their excellent thermal performance. To evaluate the enhancement effect of nanofluids, Fig. 12 shows the comparison of deionized water and nanofluids on pressure drop, Nusselt number, and overall efficiency.

It can be seen that as the Reynolds number increases, the pres-

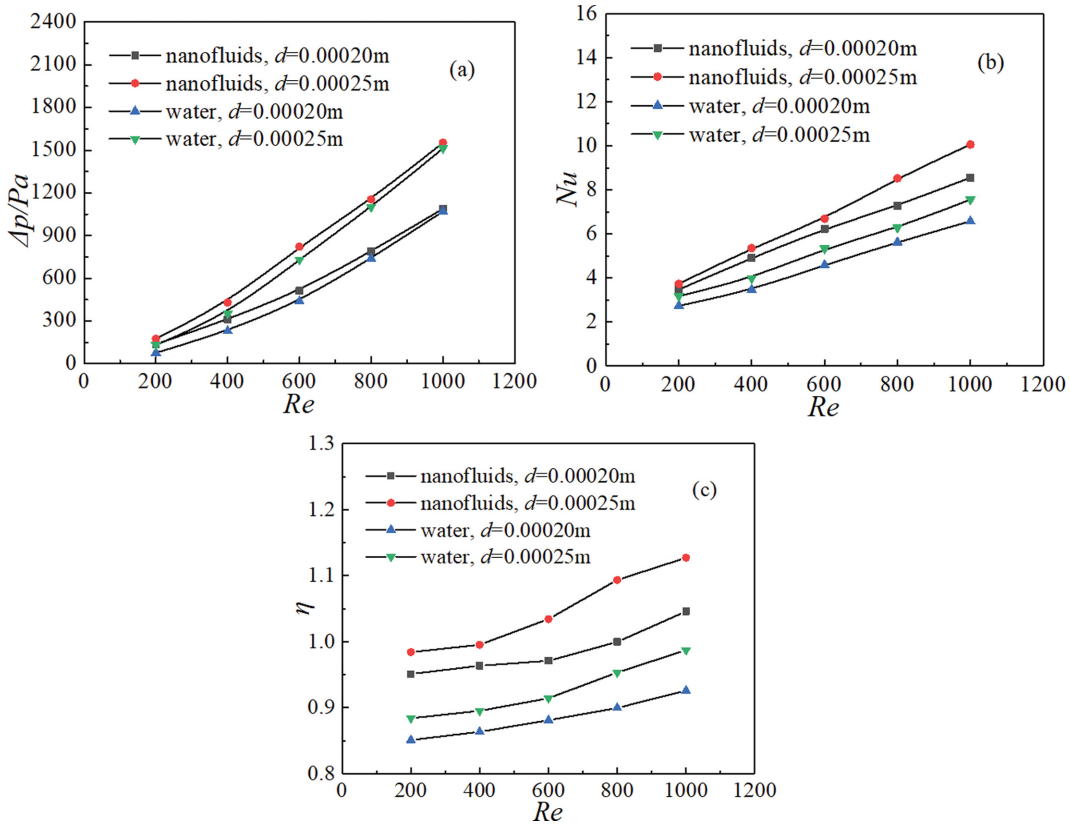

Fig. 12. Comparison of water and nanofluids at e=0.2. (a) Pressure drop versus Re, (b) Nu versus Re, (c) η versus Re.

sure drop brought by both water and nanofluids is increasing, but the change rate of the pressure drop rise curve is greater when water is the working fluid. Since water has lower viscosity, the pressure drop brought by water is smaller than that brought by nanofluids. However, as the Reynolds number increases, the effect of the traveling rib on the reduction of pressure drop becomes more pronounced for nanofluids, which is because nanofluids with higher viscosity can carry out the interruption and recomposition of the boundary layer more consistently. Although the flow boundary layer of water can continue to generate some disturbance after the destruction, the heat transfer capacity of nanofluids is stronger than that of water, which leads to that the Nusselt number of the nanofluids coupled with fractal microchannel is 42% higher than that of the deionized water coupled with fractal microchannel at most.

As a result, the overall efficiency of the nanofluids coupled with fractal microchannel is 11.54% to 13.74% higher than that of the deionized water coupled with the fractal microchannel. Even the overall efficiency of the deionized water coupled with fractal microchannel does not exceed 1 under the experimental Reynolds number range (Re=200-1,000).

CONCLUSIONS

A novel bionic fractal microchannel heat sink with traveling-wave fins based on fractal theory and disk-like tree-like structure has been developed. Thermo-hydraulic performance of nanofluids in the bionic fractal microchannel heat sink with traveling-wave fins was simulated numerically, and its comprehensive performance was also studied. The following conclusions are drawn:

(1) The fractal channel will have a fractal effect on TMHS, resulting in higher heat transfer performance on the inside of the channel and lower thermal exchange performance on the outside of the channel, coupling into the traveling wave ribs can effectively improve this problem and achieve temperature homogeneity.

(2) TMHS with traveling ribs promotes the change of flow continuity and the continuous interruption and recomposition of the thermal boundary layer, which efficiently enhances the thermal exchange, and the thermal exchange performance varies with the eccentricity ratio of the traveling ribs. As the eccentricity ratio increases, the Nusselt number first increases by 1.19% to 2.27% and then decreases by 2.10% to 5.58%, reaching a maximum at an eccentricity ratio of 0.1.

(3) Due to the special characteristics of the traveling wave ribs, the destruction and regeneration of the boundary layer have a faster response rate and smoother regeneration, so it can effectively control the viscous resistance at the bottom of the traveling wave and achieve a certain effect of reducing the pressure drop. With the increase of eccentricity ratio, the reduction effect of pressure drop can be improved from 8.81% to 13.63%.

(4) In the range of Reynolds number in this study (Re=200-1,000), the comprehensive performance index varies with the depth of traveling wave ribs, eccentricity ratio, and overall Reynolds number, while the best comprehensive performance is achieved when the working fluid is nanofluid, the eccentricity ratio is 0.1 or 0.2,

and the depth is 0.00020 m or 0.00025 m.

(5) In this paper, a novel TMHS with a working fluid of α-Al_2O_3-water nanofluids is proposed, which achieves better temperature homogeneity in the channel and on the heated surface, and at the same time it has a high overall heat transfer efficiency. It can be applied to the heat dissipation design of small electronic components or small heat-generating devices, providing a new idea for the development of a microchannel heat sink.

ACKNOWLEDGEMENTS

This work is financially supported by National Natural Science Foundation of China (Grant No. 51606214) and Natural Science Foundation of Jiangsu Province, China (Grant No. BK20181359).

NOMENCLATURE

A : area of the panel [m^2]
C_p : specific heat capacity [$J/kg^{-1}\cdot K$]
d_0 : diameter of the smooth microchannel [m]
D : hydraulic diameter [m]
e : eccentricity ratio of traveling wave fins
E : distance between the deepest point of the structure and the center of the structure [m]
h : convective heat transfer coefficient [$W/m^{-2}\cdot K$]
h_0 : height from the peak to the trough of the traveling wave structure [m]
H : height of the microchannel [m]
Kn : Knudsen number
L : length of the microchannel [m]
L_0 : length of the first level microchannel [m]
L_1 : length of the second level microchannel [m]
L_2 : length of the third level microchannel [m]
L_3 : distance between traveling wave fin structures [m]
m : mass flow rate [kg/s]
M : width between the peaks of the structure [m]
MHS : microchannel heat sink
n_v : molecules per unit volume
Nu : Nusselt number
P : pressure [Pa]
ΔP : pressure drop [Pa]
q : heat flux [W/m^2]
Q : quantity of heat [W]
R : radius of disk-shaped TMHS [m]
Re : Reynolds number
R_{in} : inlet radius [m]
T : temperature [K]
ΔT : temperature rise [K]
TMHS : tree-shape microchannel heat sink
u : inlet velocity [m/s]
U : volume flow rate [m^3/s]
V : velocity [m/s]
W : width of the microchannel [m]

Greek Symbols

θ : fractal angle of TMHS [rad]
λ : thermal conductive [W/m·K]
λ_m : mean free path [m]
μ : kinetic viscosity of fluid medium [Pa·s]
ν : velocity vector [m/s]
ρ : density of liquid water [kg/m^3]
w : width difference [mm]

Subscripts

c : cavity
f : fluid
in : inlet
out : average of outlets
pum : pumping power
r : rib
s : solid
sm : smooth wall surface
w : wall of the microchanne

REFERENCES

1. H. Li, Y. He, C. Wang, X. Wang and Y. Hu, *Appl. Therm. Eng.*, **236**, 117 (2019).
2. M. Chen, X. Wang, Y. Hu and Y. He, *J. Quant. Spectrosc. Ra.*, **250**, 107029 (2020).
3. K. G. Dehkordi, A. Karimipour, M. Afrand, D. Toghraie and A. H. M. Isfahani, *Int. J. Thermophys.*, **41**, 132 (2020).
4. M. Sheikholeslami, M. B. Gerdroodbary, S. V. Mousavi, D. D. Ganji and R. Moradi, *J. Magn. Magn. Mater.*, **460**, 302 (2018).
5. D. B. Tuckerman and R. F. W. Pease, *IEEE. Electr. Device. L.*, **2**(5), 126 (1981).
6. S. A. Sajadifar, A. Karimipour and D. Toghraie, *Eur. J. Mech. B-Fluid.*, **61**, 25 (2017).
7. S. Rostami, H. Ahmadi-Danesh-Ashtiani, D. Toghraie and R. Fazaeli, *Physica A.*, **548**, 123879 (2020).
8. C. Hua, X. Wang, X. Gao, H. Zheng, X. Han and G. Chen, *Appl. Therm. Eng.*, **126**, 1058 (2017).
9. Z. Li, A. Shahsavar, K. Niazi, A. A. Al-Rashed and S. Rostami, *Int. Commun. Heat Mass.Transf.*, **115**, 104628 (2020).
10. S. U. Choi and J. A. Eastman, *ASME-Publications-Fed*, **231**, 99 (1995).
11. M. Bahiraei, N. Mazaheri and H. Moayedi, *Int. J. Heat. Mass Transf.*, **151**, 119419 (2020).
12. A. Kumar, V. Sugunamma, N. Sandeep and and R. Ramana, *Multidiscip. Model. Mater. Struct.*, **15**(1), 103 (2018).
13. M. Sheikholeslami and S. Abelman, *Eng. Computation.*, **35**(5), 1855 (2017).
14. M. Izadi, B. Bastani and M. A. Sheremet, *Adv. Powder Technol.*, **31**(6), 2493 (2020).
15. D. H. Werner and S. Ganguly, *IEEE. Antenn. Propag. M.*, **45**(1), 38 (2003).
16. A. Bejan and M. R. Errera, *Fractals.*, **5**(04), 685 (1997).
17. A. Bejan, *J. Heat Transf.*, **122**(3), 430 (2000).
18. D. V. Pence, *Nanosc. Microsc. Therm.*, **6**(4), 319 (2003).
19. M. Varmazyar, M. Habibi, M. Amini, A. H. Pordanjani, M. Afrand and S. M. Vahedi, *Powder Technol.*, **366**, 164 (2020).
20. W. He, R. Mashayekhi, D. Toghraie, O. A. Akbari and I. Tlili, *Int.*

Commun. Heat Mass Transf., **117**, 104700 (2020).
21. Y. Chen and P. Cheng, *Int. J. Heat. Mass Transf.*, **45**(13), 2643 (2002).
22. P. Ma, T. Fu, C. Zhu and Y. Ma, *Korean J. Chem. Eng.*, **36**(1), 21 (2019).
23. L. Zhang, D. Peng, W. Lyu and F. Xin, *Chem. Eng. J.*, **263**, 452 (2015).
24. D. R. Emerson, K. Cieślicki, X. Gu and R. W. Barber, *Lab Chip.*, **6**(3), 447 (2006).
25. M. Izadi, S. H. Pour, A. K. Yasuri and A. J. Chamkha, *J. Therm. Anal. Calorim.*, **136**, 2461 (2019).
26. M. Bahiraei and A. Monavari, *Appl. Therm. Eng.*, **179**, 115621 (2020).
27. K. Bao, C. Hua, X. Wang, X. Han and G. Chen, *Int. J. Heat. Mass Transf.*, **154**, 119672 (2020).
28. P. Talebizadehsardari, H. Rahimzadeh, G. Ahmadi, K. Inthavong, M. M. Keshtkar and M. A. Moghimi, *Adv. Powder Technol.*, **31**(8), 3134 (2020).
29. S. Rostami, A. Aghaei, A. H. Joshaghani, H. M. Hezaveh, M. Sharifpur and J. P. Meyer, *J. Therm. Anal. Calorim.*, **143**, 1569 (2021).
30. A. Arshad, M. Jabbal, P. T. Sardari, M. A. Bashir, H. Faraji and Y. Yan, *Therm. Sci. Eng. Prog.*, **18**, 100520 (2020).
31. C. Herman and E. Kang, *Int. J. Heat Mass Transf.*, **45**(18), 3741 (2002).
32. C. Qi, T. Chen, J. Tu and Y. Wang, *Korean J. Chem. Eng.*, **37**(12), 2104 (2020).
33. A. M. Guzmán, M. J. Cárdenas, F. A. Urzúa and P. E. Araya, *Int. J. Heat Mass Transf.*, **52**(15-16), 3778 (2009).
34. D. Y. Kim and J. M. Kim, *Korean J. Chem. Eng.*, **36**(6), 837 (2019).
35. C. Qi, T. Chen, Y. Wang and L. Yang, *Korean J. Chem. Eng.*, **37**(9), 1466 (2020).
36. C. Qi, J. Hu, M. Liu, L. Guo and Z. Rao, *Energ. Convers. Manage.*, **153**, 557 (2017).
37. S. R. Yan, A. Golzar, M. Sharifpur, J. P. Meyer, D. H. Liu and M. Afrand, *Int. J. Mech. Sci.*, **185**, 105832 (2020).
38. M. W. Tian, S. Rostami, S. Aghakhani, A. S. Goldanlou and C. Qi, *Int. J. Mech. Sci.*, **189**, 105975 (2021).
39. Z. Li, M. Sheikholeslami, M. Jafaryar, A. Shafee and A. J. Chamkha, *J. Mol. Liq.*, **266**, 797 (2018).
40. Y. Hu, L. Shi, Z. Zhang, Y. He and J. Zhu, *Energ. Convers. Manage.*, **213**, 112829 (2020).
41. H. Li, Y. He, X. Wang, D. Liu and Z. Liu, *J. Alloy. Compd.*, **773**, 743 (2019).
42. M. Sheikholeslami, A. Arabkoohsar, I. Khan, A. Shafee and Z. Li, *J. Clean. Prod.*, **221**, 885 (2019).
43. D. M. C. Shastry and U. C. Arunachala, *J. Energy Storage*, **28**, 101312 (2020).
44. X. Wang, Y. Li, Y. Yan, E. Wright, N. Gao and G. Chen, *Int. J. Refrig.*, **119**, 316 (2020).
45. M. Eisapour, A. H. Eisapour, M. J. Hosseini and P. Talebizadehsardari, *Appl. Energ.*, **266**, 114849 (2020).
46. H. M. Sandeep and U. C. Arunachala, *Renew. Sust. Energ. Rev.*, **69**, 1218 (2017).
47. Y. Peng, W. Liu, W. Chen and N. Wang, *Int. J. Heat Mass Transf.*, **71**, 79 (2014).
48. F. Fan, C. Qi and Q. Liu, *Case. Stud. Therm. Eng.*, **22**, 100761 (2020).
49. C. Qi, Y. Wang and J. Tang, *Asia-Pac. J. Chem. Eng.*, **15**(4), e2482 (2020).
50. W. Yan, C. Li and W. Ye, *Heat Transf. Asian Res.*, **48**, 2329 (2019).
51. D. Ma, G. Xia, J. Wang, Y. Yang, Y. Jia and L. Zong, *Energ. Convers. Manage.*, **152**, 157 (2017).
52. Y. Li, R. Kalbasi, Q. Nguyen and M. Afrand, *Powder Technol.*, **367**, 464 (2020).
53. S. Rostami, M. Zarringhalam, A. A. Alizadeh, D. Toghraie and A. S. Goldanlou, *J. Mol. Liq.*, **312**, 113130 (2020).
54. A. Karimipour, A. D'Orazio and M. S. Shadloo, *Physica E.*, **86**, 146 (2017).
55. K. A. Kumar, J. R. Reddy, V. Sugunamma and N. Sandeep, *Alex. Eng. J.*, **57**, 435 (2018).
56. M. Izadi, M. Javanahram, S. M. H. Zadeh and D. Jing, *Chinese J. Chem. Eng.*, **28**(2), 329 (2020).